Title

A multimodal magnetoelastic artificial skin for underwater haptic sensing.

Journal

Science Advances, 10(1)

Authors

Zhou, Yihao

Zhao, Xun

Chen, Guorui

et al.

Publication Date

2024-01-05

DOI

10.1126/sciadv.adj8567

Peer reviewed

APPLIED SCIENCES AND ENGINEERING

A multimodal magnetoelastic artificial skin for underwater haptic sensing

Yihao Zhou†, Xun Zhao†, Jing Xu, Guorui Chen, Trinny Tat, Justin Li, Jun Chen*

Future exploitation of marine resources in a sustainable and eco-friendly way requires autonomous underwater robotics with human-like perception. However, the development of such intelligent robots is now impeded by the lack of adequate underwater haptic sensing technology. Inspired by the populational coding strategy of the human tactile system, we harness the giant magnetoelasticity in soft polymer systems as an innovative platform technology to construct a multimodal underwater robotic skin for marine object recognition with intrinsic waterproofness and a simple configuration. The bioinspired magnetoelastic artificial skin enables multiplexed tactile modality in each single taxel and obtains an impressive classification rate of 95% in identifying seven types of marine creatures and marine litter. By introducing another degree of freedom in underwater haptic sensing, this work represents a milestone toward sustainable marine resource exploitation.

INTRODUCTION

Approximately 70% of the Earth's surface is covered by water, primarily in the form of oceans, which play a crucial role in regulating global climate and are home to a vast array of valuable but underexplored resources including deep-sea minerals (*1*) and diverse biological species (*2*). As terrestrial resources are gradually depleted and scarce, marine resources are becoming increasingly indispensable. However, marine resource exploitation has been hindered by their inaccessibility and the escalated development cost associated with the hypoxia, corrosion, and high-pressure nature of the ocean environment, which makes it challenging for humans to access (*3*). To exploit marine resources, advanced technologies such as intelligent autonomous underwater robotics (AURs) with human-level dexterity are essential. However, the deployment of such AURs is heavily dependent on the availability of underwater haptic sensing technology, which has remained a grand challenge in the community.

Various haptic sensing technologies have been developed using different transduction mechanisms such as piezoresistance (*4*), capacitance (*5*), optics (*6*), piezoelectricity (*7*), and triboelectricity (*8*). Through the assistance of machine learning algorithms, these sensors have been used with a broad range of applications for object and texture recognition (*4*, *9*), dexterous manipulation (*10*), adaptive grasping (*11*), and human-machine interface (*12*). However, many of the tactile sensing mechanisms are vulnerable to water or even humidity, which limits their usefulness in the underwater environment (*13*), especially with hydrostatic pressure. In addition, to achieve human-level dexterity, haptic sensors must decode complex mechanical information including force type, magnitude, and direction, in each taxel, while maintaining a high taxel density. Existing tactile sensors typically use three to four channels to realize force-decoupling capability within a single taxel, which results in a complex structure and requires both intricate front-end and back-end circuits (*14*). A haptic sensing system capable of achieving multiplexed tactile modality within a single taxel, while also offering intrinsic waterproofness and a simple configuration, is now unavailable and in high demand for underwater haptic sensing.

Skin is the largest human somatosensory system and is composed of three primary layers: the epidermis, the dermis, and the hypodermis (*15*). Four primary tactile mechanoreceptors are distributed hierarchically inside the dermis and hypodermis (*16*, *17*). When an external touch stimulation is applied, the tactile information, including the normal force magnitude, the shear force magnitude, the shear force direction, and the object shape, is delivered through mechanical deformation to the mechanoreceptors, which are essentially nerve endings of the sensory neurons. Then, all the information is transmitted to and decoded in the sensory cortex inside the brain. A principal feature of the human tactile sensing mechanism is that each primary afferent can terminate on several receptors with different receptive fields and the rich tactile information is encoded by the population response of all afferents on the periphery of the stimulation area instead of a single one (*18*). As a result, human tactile perception and cognition is a natural encoding-decoding process through a collective behavior of multiple sensory "channels." This encoding-decoding paradigm of the human tactile system is a remarkable testament to biological evolutions, providing heightened sensory resolution, accuracy, and robustness.

Here, we present a somatosensory system–inspired, intrinsically waterproof, chemically stable, and mechanically durable artificial skin with perception-to-cognition intelligence for underwater haptic sensing by exploiting magnetoelasticity in a soft magnetoelastic elastomer. The developed bioinspired magnetoelastic artificial skin (BMAS) has a hierarchical structure compromising an untethered magnetomechanical coupling (MC) layer and two stackable magnetic induction (MI) sensing layers to imitate the hierarchically layered structure of the human somatosensory system. Tactile stimuli on the MC layer are converted into magnetic field variations, which are not subject to intensity loss in the aquatic environment because the magnetic field could penetrate water. These magnetic field variations will then be converted into analyzable electrical signals by the population response of the sensory channels in the MI layers, which mimic the collective behavior of the human tactile system. A one-dimensional convolutional neural network (1D-CNN) was further used to decode the electrical signals, providing critical information

Department of Bioengineering, University of California, Los Angeles, Los Angeles, CA 90095, USA.
*Corresponding author. Email: jun.chen@ucla.edu
†These authors contributed equally to this work.

for natural shear and normal force decoupling. As a result, a single pixel can gain a multiplexed touching modality and a three-dimensional (3D) force refactoring, achieving an accuracy of 95% in distinguishing normal force, shear forces, tapping, and vibration. Toward practical application, a waterproof haptic sensing system was developed with the BMAS for marine object recognition. It achieves a classification rate of 95% in recognizing seven types of marine creatures and marine litter. The potential applications extend beyond marine litter recycling, with opportunities for deep-sea biological sampling and other tactile-based systems. With a collection of compelling features, including bioinspired characteristics, simple structure, low cost, high scalability, and a self-powered working manner in aquatic environments, the BMAS-based haptic sensing system represents a reliable technology platform for underwater tactile perception and cognition and a key step toward the ultimate goal of sustainable and eco-friendly marine resource exploitation.

RESULTS

Bioinspired magnetoelastic artificial skin

The prior requirement of the underwater haptic sensing system is that its sensing mechanism must be insusceptible to water and the aquatic environment. In addition, for maximum utility, the system should be adaptable to various types of AURs and capable of supporting a range of complex underwater exploration tasks, including biological sampling, infrastructure inspection and maintenance, marine litter recycling, deep-sea mining, and fishing (Fig. 1A). Thus, the design principle for the underwater haptic sensing system consists

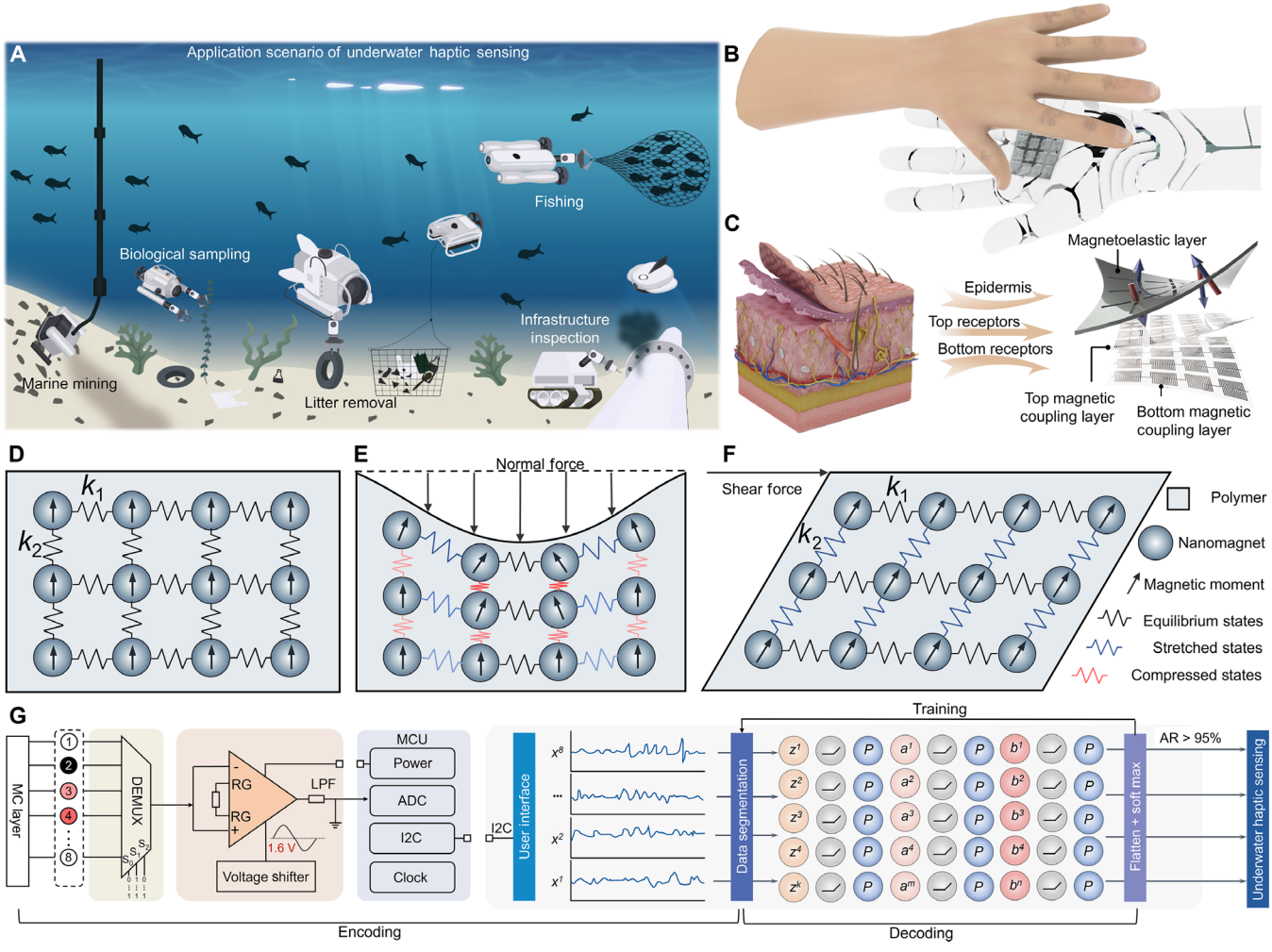

Fig. 1. Overview of the BMAS-based underwater haptic sensing. (**A**) The future exploitation of marine resources will encompass a range of activities including deep-sea biological sampling, mining, seafloor litter removal, and construction and maintenance of underwater infrastructure. To achieve these goals, autonomous underwater robots equipped with advanced haptic sensing capabilities will play a crucial role. (**B**) The untethered MC layer mimics the signal transmission functionality of the epidermis and dermis layers of human skin in response to applied tactile pressure. The two MI sensing layers resemble the tactile mechanoreceptors that are hierarchically distributed in the dermis. The sensation of amplitude, location, and type of the applied pressure on the artificial skin is realized by the cooperative response of multiple nearby coil pixels instead of a single one, which is imitating the human tactile sensing mechanism. (**C**) Illustration of the three layers of the magnetoelastic haptic sensing system. (**D** to **F**) Mechanism of the MC layer to distinguish the normal and shear force. Normal (E) and shear forces (F) yield a different magnetic field response, which can be picked by multiple sensory channels of the MI layer. k_1 and k_2 refers to effective elastic constant of the polymer matrix. (**G**) The customized circuit and algorithm design to mimic the encoding-decoding process of the human tactile system to realize multichannel magnetoelastic tactile perception and cognition.

of two main steps. The first step involves selecting a sensing mechanism that is well suited to the unique challenges of the aquatic environment. The second step involves designing a device architecture that can replicate the capabilities of human skin to achieve high levels of multimodality and dexterity. Motivated by the mechanism of human tactile sensing (Fig. 1B), we create a BMAS that is soft and can conformably attach to the human body and curved robotic arms (fig. S1). It consists of three layers: an untethered MC layer and two hierarchical MI layers (Fig. 1C). The 4 cm–by–4 cm–by–0.35 cm MC layer is composed of neodymium-iron-boron (NdFeB) nanomagnets and a silicone rubber matrix with a weight ratio of 1:1. As shown in the scanning electron microscopy in fig. S2 (A and B), the distribution of NdFeB nanomagnets features an average interparticle distance of 20.79 μm and an SD of 10.26 μm. The MC layer mimics the signal generation and transmission functionality of the epidermis and dermis of the human skin for the applied tactile stimulation. Twenty-four orthogonal grooves divided the MC layer into 16 pixels, as illustrated in fig. S3. In addition, the magnetic field of the MC layer is spatially programmed to enable a diagonal distribution of north and south poles using an origami configuration during impulse magnetization. The two MI layers are composed of in-plane conductive tracks and can be regarded as the mechanoreceptors in our BMAS system. As illustrated in fig. S4A, the top induction layer contains four sensory channels in parallel, and each channel includes four serially connected coil sensing elements (1 cm by 1 cm). To enable the series connection, a double-sided configuration is adopted with two sensing coils on the front, the other two on the back, and four vertical-interconnected accesses bridging them together (fig. S4, B and C). The bottom induction layer resembles the top layer but orients in an orthogonal direction (fig. S4, D to F). In terms of functionality, the MC layer uses the recently discovered giant magnetoelastic effect in the soft material systems (*19*) to convert the mechanical deformation into magnetic flux density variation through magnetic particle-particle interactions. The two MI layers play the role of converting the magnetic flux density changes from the MC layer into processable electric signals through Faraday's law of induction.

The BMAS design exhibits two distinctive characteristics that differentiate it from other tactile sensing devices now available. First, it leverages the long-range property of the magnetic field, allowing the variation of the magnetic field generated by tactile stimulation on the MC layer to be detected by multiple stackable MI layers. This implies that while the prototype of the BMAS includes two MI layers, more MI layers can be readily stacked into the system. By altering the design of the MI layer number, the sensory channels in each MI layer, and the properties of coil sensing elements, such as their distributions and sizes, different levels of tactile perception can be achieved, resulting in enhanced accuracy and adaptivity to different tactile tasks (fig. S5). Thus, this feature introduces a previously unidentified concept of a 3D stackable haptic sensor, distinguishing the BMAS from prior tactile sensors that were limited to a planar electrode arrangement (note S1). It opens another degree of freedom in the design of tactile sensory channels and better mimics the layered structure of the human somatosensory system, in which mechanoreceptors are distributed hierarchically in different layers. Second, the design of a single sensory channel with multiple coil sensing elements in the MI layers mimics the populational encoding strategy of the human afferent innervating multiple mechanoreceptors. Therefore, the magnetoelastic artificial skin uses the populational response of multiple adjacent sensory channels across various taxels to encode the tactile information analog to the human tactile sensing system. This is distinct from previous tactile sensors that rely on sensory channels within a single pixel to perform encoding. This design can substantially reduce the number of sensory channels in the haptic sensor and simplify sensor architecture while preserving all tactile information. In this BMAS prototype, rich information on tactile stimuli including press and shear in different directions can be encoded by the populational response of multiple channels in the orthogonal MI layers. As a result, eight sensory channels with a configuration of 4 by 4 could accomplish the task of a conventional tactile sensor that holds 64 channels (4 by 4 by 4), substantially reducing the data acquisition complexity.

The ability of the BMAS to decouple normal and shear forces relies on encoding the different magnetic field variations caused by the different tactile stimuli in the MC layer into populational sensory signals in the MI layer. As illustrated in Fig. 1D, the MC layer is in an equilibrium state where the magnetic particle-particle interactions are balanced by the elasticity of the polymer matrix. When subjected to different tactile stimulations, such as normal and shear forces, the arrangement and magnetization of the nanomagnets can exhibit dissimilar alterations (Fig. 1, E and F), which, in turn, results in distinctive magnetic field variations within the MI layers. Simultaneously, the interparticle polymer matrix undergoes compression or stretching, enabling it to store elastic energy that is subsequently released to return the MC layer to its equilibrium state following the cessation of external tactile stimulation. In this process, the BMAS encodes tactile information of different pixels into unique electrical signals for the subsequent decoding process. The grooved structure and programmed magnetization design of the MC layer aim to mitigate cross-talk interference of the normal press while amplifying shear movement in a single pixel, which results in a more distinct magnetic field variation from these tactile stimuli within the MC layer and helps promote the subsequent recognition accuracy (*20*).

The converted electrical signals in various sensory channels are then demultiplexed, amplified, filtered, processed by a custom-designed circuit, and then fed into an artificial neural network imitating the human brain for the decoding of tactile information (Fig. 1G). The decoded tactile information from the 1D-CNN such as the amplitude, location, type of the applied pressure, and shape and texture of the contacting object is lastly used for underwater haptic sensing toward the sustainable exploitation of marine resources.

Pressure perception capability characterization

The designed BMAS is initially characterized for pressure perception capability through a comprehensive analysis of its mechanical properties, magnetoelastic behavior, and electrical performance. Figure 2A demonstrates the stress-strain curve of the MC layer in the BMAS under uniaxial stretch. It is clear that a 330% stretchability can be ensured even with the groove structure design. A Young's modulus of 101.096 kPa is derived using the neo-Hookean model, which is in the same order as the human skin. The advantage of the groove design is confirmed by the finite element simulation. As depicted in Fig. 2B, a 20-kPa normal stress on the unstructured MC layer (7 mm by 7 mm) causes a circular displacement field substantially extended to the nearby pixels with a measured value of ~22 μm. On the contrary, when the same stress is applied to the MC layer equipped with orthogonal groove structures, the displacement field is effectively contained within a single pixel, with the surrounding pixels only

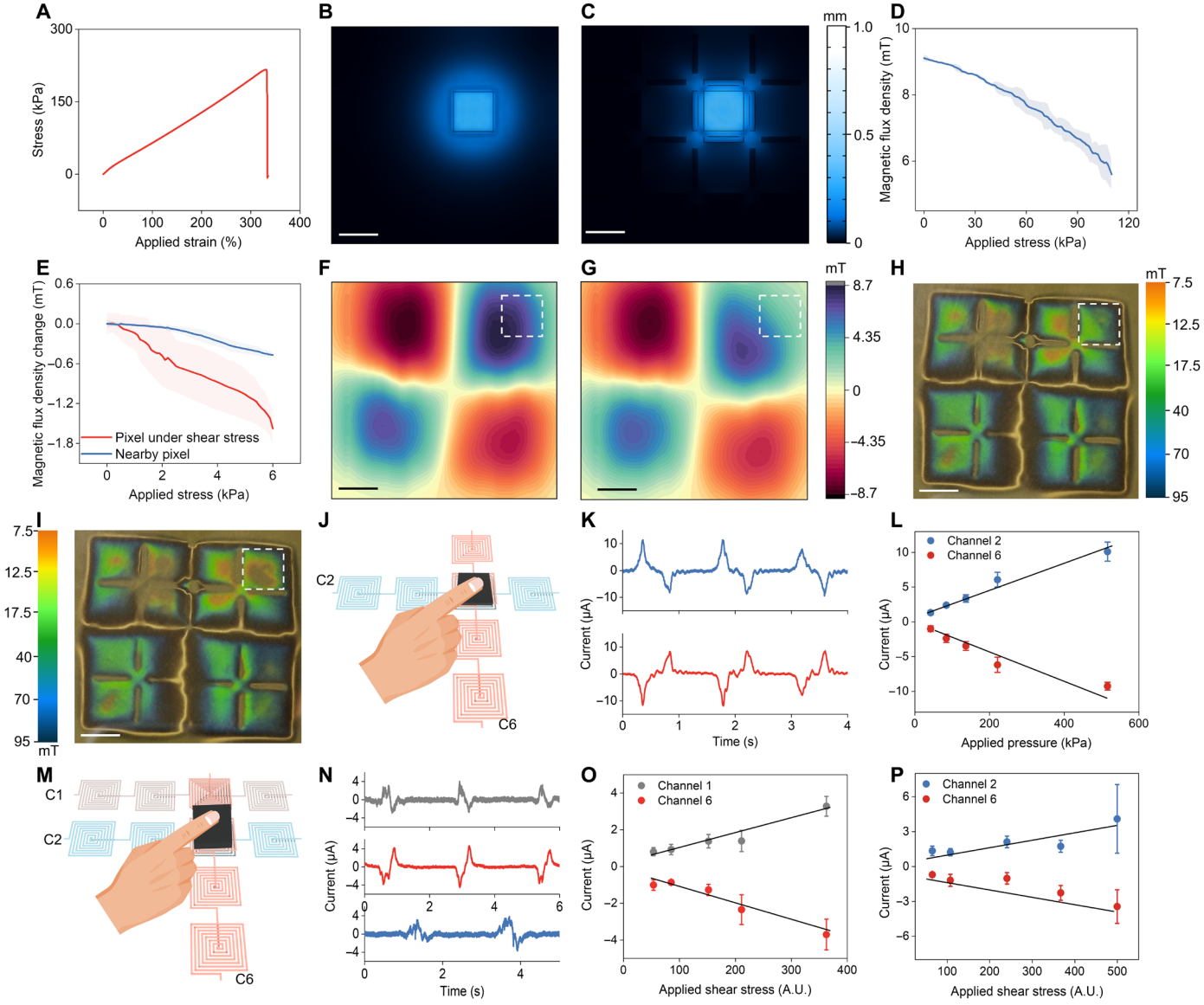

Fig. 2. Magnetic, mechanical, and electrical characterization of the magnetoelastic artificial skin. (**A**) Stress-strain curve of the MC layer. (**B**) Displacement field of the unstructured MC layer when 20 kPa is applied to a pixel. Scale bar, 1 cm. (**C**) Displacement field of the groove-structured MC layer when 20 kPa is applied to a pixel. Scale bar, 1 cm. (**D**) Magnetic flux density versus applied normal stress at the center of a pixel. Data are means ± SD; $N = 3$. (**E**) Magnetic flux density variation versus applied shear stress at the center of a pixel and its nearby pixel. Data are means ± SD; $N = 3$. (**F**) Mapping of the *Z*-axis magnetic flux density at 0 kPa. Scale bar, 1 cm. (**G**) Mapping of the *Z*-axis magnetic flux density with 200 kPa applied to the white dashed box. Scale bar, 1 cm. (**H**) Mapping of the magnetic flux density using a magnetic flux display. Scale bar, 1 cm. (**I**) Mapping of the magnetic flux density with a pressing force of 5 N on the white dashed box using a magnetic flux display. Scale bar, 1 cm. (**J**) Illustration of normal stress on a single pixel and two sensory channels are excited. (**K**) Signal waveform in channel 2 and channel 6 under normal stress of 515.87 kPa. (**L**) Sensitivity of channel 2 and channel 6 under normal stress. Data are means ± SD; $N = 5$. (**M**) Illustration of shear stress on a single pixel and when three sensory channels are excited. (**N**) Signal waveform in channel 2, channel 6, and channel 1 under shear stress. (**O**) Sensitivity of channel 1 and channel 6 under shear stress. Data are means ± SD; $N = 5$. (**P**) Sensitivity of channel 2 and channel 6 under shear stress. Data are means ± SD; $N = 5$. A.U., arbitrary units.

experiencing an 11-μm displacement (Fig. 2C). This result highlights the exceptional ability of grooves to mitigate the cross-talk during normal presses. The groove design not only mitigates the cross-talk of normal stress but also facilitates the shear deformation of each single pixel. Figure S6 compares the simulated deformation fields of the MC layer with and without groove structures under a shear stress of 2 kPa. It can be seen that a displacement of 134 μm can be acquired in the groove-structured MC layer, whereas only 60 μm is obtained at the same point in the unstructured MC layer. By mitigating the cross-talk of the normal press while facilitating that of shear deformation, the groove structure is proven to promote the natural decoupling of normal and shear tactile information in the BMAS.

The magnetoelastic effect of the BMAS at the center of a single pixel is investigated by a customized measurement platform, and the relationship between the magnetic flux density and the applied

stress is depicted in Fig. 2D. It can be seen that the magnetic flux density decreases with increasing stress and a high value of the magnetic flux density variation of 3 mT can be obtained with applied stress of 102.8 kPa, corresponding to an MC factor of 2.91×10^{-8} T Pa^{-1}. Besides the applied normal stress, the magnetic flux density variation of the BMAS under shear stress is further examined at the center of the sheared pixel and its nearby pixel in the shear direction as schemed in fig. S7A. As demonstrated in Fig. 2E, the magnetic flux density decreases at both positions and the pixel under the shear stress displayed a larger magnetic field variation. The shear deformation transpires within the subarray characterized by identical magnetization polarity. Given that the magnetization profile of the MC layer is programmed in a diagonal manner, shearing deformation may similarly manifest within the subarray of opposite polarities, as illustrated in fig. S7B. This situation was also examined, and the result presented in fig. S7C demonstrates the magnetic flux density on the surface of a pixel when its neighboring pixel, with an opposite magnetization polarity, is sheared toward it. Notably, an increase in magnetic flux density is observed in stark contrast with the shear deformation scenario in the subarray of identical magnetization polarity. Thus, it is concluded that shear deformation will cause a negative (positive) magnetoelastic effect in the neighboring pixel (in the shear direction) when the sheared and neighboring pixels have uniform (opposite) polarity. Beyond the magnetic flux density variation at a single point, the mapping of the *Z*-axis magnetic flux density of the BMAS is also investigated, and the result is shown in Fig. 2F. It is clear that the south and north poles distribute along the diagonal of the BMAS, confirming the programmed magnetization design. In addition, when normal stress of 200 kPa is applied to the single pixel (marked by the white dashed line), a notable decrease of the magnetic flux density in the whole area can be observed (Fig. 2G), in line with the result in Fig. 2D. Taking a step further, the magnetoelastic effect of the MC layer is visualized and better confirmed by a magnetic flux display. As illustrated in Fig. 2 (H and I), fig. S8, and movie S1, a pressing force of 5 N can substantially reduce the magnetic flux density of a taxel evidenced by the color change (from green to red) of the magnetic flux display. A key feature of the BMAS is that it uses the deep penetration depth of the magnetic field and the magnetoelastic effect. This design allows multiple MI layers to collect the variation of magnetic flux density generated by the MC layer simultaneously. While previous characterizations focused on the surface magnetic flux density variation of the MC layer, additional experiments were performed to investigate the penetration depth of the magnetic field and the magnetoelastic effect, with the results displayed in fig. S9. Notably, the penetration depth and decay of the magnetoelastic effect are measured to be approximately 3.69 mm and 4% per 220 μm (thickness of the MI layer substrate), indicating that more than 10 MI layers can perceive the magnetoelastic effect of the MC layer simultaneously, although with a gradually decreased intensity.

The different magnetic field variations of the BMAS under normal and shear stress are a representation of different magnetoelastic effects under different mechanical stimuli, which encodes vital information for the BMAS to distinguish different tactile information such as the normal force, shear force, object shape, and object movement. The variation of the magnetic flux density caused by the magnetoelastic effect is then converted into high-fidelity and analyzable electrical signals by the stackable MI layers in the BMAS. We first investigate the output characteristics of a single pixel under different tactile stimulation using sensory channels within its receptive field. As illustrated in Fig. 2J, when the normal stress is applied to a single pixel, sensory channel 2 and channel 6 under the stress will generate current signals. With applied normal stress of 515.87 kPa, a complete waveform in a single channel is found to include two consecutive current peaks at the level of 10 μA with opposite directions corresponding to the press and release processes during one touch (Fig. 2K). It should be noted that the current signals in channel 2 and channel 6 have different directions due to the different connections of the top and bottom MI layers. This design provides valuable information to distinguish the stacked MI layers and contributes to the improved cognition of the BMAS. Figure 2L presents the relationship between the current output and applied normal stress in channel 2 and channel 6. A linear correlation can be observed for both channels, indicating the capability of the artificial skin to perceive the magnitude of the applied normal force. It is noteworthy that the current amplitudes obtained from channel 2 and channel 6 in both Fig. 2K and Fig. 2L align with each other, indicating that the magnetic flux density variations perceived by the two stacked MI layers are similar. This point holds notable importance, as it suggests minimal signal or information loss due to the stacked structure. This characteristic distinguishes the proposed sensor from previous multilayer capacitive sensors, which have exhibited substantial information loss due to the stacked layers (*21*). To provide an exhaustive analysis of the signal intensity disparities between the top and bottom MI layers, the peak values of 30 current signals in channel 2 and channel 6, elicited from a press deformation on an individual pixel, were meticulously documented and subjected to rigorous statistical analysis (fig. S10). The results show that the electrical signal in the bottom MI layer is 4.8% smaller than that in the top MI layer. The subtle variance in the peak current between the top and bottom MI layers aligns with, and can be attributed to, the 4% diminution of the magnetoelastic effect per MI layer. Essentially, the bottom MI layer is positioned at a greater distance from the MC layer relative to the upper MI layer, leading to a slightly decreased peak current. Nonetheless, the current profiles obtained by the two MI layers demonstrate notable parallelism, ensuring that the layered architecture introduces only a minimal compromise in information transmission fidelity. Figure 2M illustrates the situation in which shear stress is applied to a single pixel in an upward direction in the subarray of identical magnetization polarity (fig. S7A). In this situation, an additional sensory channel in the direction of the shear deformation (e.g., channel 1) will perceive the magnetic flux density variation from the magnetoelastic effect of the MC layer and excite a current signal as shown in Fig. 2N. Compared to the situation of normal stress in Fig. 2J, the current signals in channel 2 and channel 6 follow an analogous waveform but have a smaller magnitude and multiple small peaks, which can be ascribed to the complexity of the shear movement. For channel 1, the direction of the current signal is the same as that obtained by channel 2, in agreement with the experimental result that the magnetic field at both pixels decreases under shear deformation. Figure 2 (O and P) presents the relationship between the current output and applied shear stress in channel 1, channel 2, and channel 6. Similar to the case of normal stress, the current magnitude increases with increasing shear stress linearly, implying the capability of the artificial skin to recognize the magnitude of applied shear force. Shear deformation may similarly manifest within subarrays of opposite magnetization polarities (fig. S7B). The electrical output from three activated channels under this

circumstance has also been analyzed, with the findings presented in fig. S11. Notably, the current directions of all three channels are reversed. The reversed current directions in channel 3 and channel 6 can be ascribed to the reversed magnetization polarity of the sheared pixel. Concurrently, the reversed current direction in channel 2 indicates an increase in the surface flux density, confirming the magnetoelastic result in fig. S7C. Apart from the normal and shear force, we also investigated the output characteristics of channel 2 and channel 6 when the single pixel above them undergoes vibration at different frequencies (fig. S12). The current output is observed to increase linearly with the applied frequency ranging from 1 to 4 Hz and 4 to 10 Hz, exploiting the rate dependency of Faraday's law.

The above mechanical, magnetic, and electrical characterizations verified the feasibility of encoding different tactile information (e.g., direction, magnitude, and type) into distinct electrical signals for a single pixel and its surrounding sensory channels in our BMAS, which is the essential foundation for the subsequent construction of a multichannel tactile interface and versatile applications. After characterizing the single pixel, we evaluate the overall performance of the BMAS using a customized circuit with a multiplexer, an amplifier, an analog-to-digital-convertor, and a microcontroller unit (MCU). In total, eight sensory channels are connected to the multiplexer, and their electrical signals are looped with a sampling rate of ~115/s per channel. The output of the multiplexer is then fed into an instrumental amplifier with a voltage shifter converting the micro-amplitude voltage signal of each sensory channel into a voltage signal at the level of 0.1 V centered on ~1.65 V. Afterward, all the electrical outputs are digitalized and processed by an MCU and displayed at the user interface. First, a normal press is exerted on all 16 pixels of the magnetoelastic artificial skin, and their resulting voltage output profiles are summarized in Fig. 3A and fig. S13. Two features of the profiles can be observed: (i) For each single press, only two orthogonal sensory channels crossing the pressed pixel exhibit notable electrical outputs, confirming the cross-talk mitigation effect of the groove design and the ability of the magnetoelastic artificial skin to distinguish 16 tactile positions using the stacked eight orthogonal "afferents." (ii) The electrical outputs correspond to the magnetic field distribution of the MC layer as evidenced by the reserved output direction in profiles of pixel 1 and pixel 3. A reconstruction of the electrical output for 16 pixels using the eight orthogonal sensory channels under the normal press on pixel 1 is illustrated in Fig. 3B. It can be observed that the peak signal intensity at pixel 1 is 200 times of the value at irrelevant pixels and 5 times of the value at pixels sharing sensory channels with pixel 1. Such high signal contrast together with the rich signal waveform ensures enough information in the perception level for an intelligent and accurate recognition. A low-pass filter can be further added for signal processing to remove the high-frequency noise and obtain a clearer output profile, as evidenced by the tactile visualization when writing the letters "U," "C," "L," and "A" in Fig. 3C. For each individual touch, the two sensory channels crossing the signal pixel respond to the touch simultaneously with a clear waveform according to the magnetization of the touch location. Beyond normal press, our BMAS can also perceive and recognize various types of tactile stimulations such as vibration, tapping, and shear deformations toward different directions at each single pixel, enabling a multiplexed touching modality while preserving a simplified device and circuit structure (Fig. 3D). For vibration and tapping, the magnitude, duration, and shape of output waveforms in the two orthogonal sensory channels apparently distinguish them from the normal press. Shear deformations toward different directions at each single pixel can excite additional sensory channels in the movement pathway benefiting from the long-range property of the magnetic field. For instance, the shear-down deformation of pixel 6 excited two additional sensory channels (channel 1 and channel 3) besides the two channels excited by the normal press (channel 2 and channel 7). Different waveforms in the additional channels encode key information to distinguish different shear deformations. In this manner, each individual pixel of our magnetoelastic artificial skin can recognize entirely seven tactile stimulations including normal press, four shear deformations, tapping, and vibration, rendering it the most complete artificial tactile skin yet with the simplest device architecture and a self-powered feature.

The pixel size of the BMAS is designed to be 1 cm by 1 cm. This size choice is drawn from an analogy between each pixel of the BMAS and a human finger knuckle, which has an estimated area of 1 to 2 cm^2. This pixel dimension allows for the possibility of localizing tactile stimuli within discrete regions of an individual pixel or at the edges between two adjacent pixels. Note S2 systematically examines the electrical output characteristics of the BMAS when tactile stimuli are applied to various positions within a single pixel and at the edge between two adjacent pixels. Experimental observations have indicated that the central region of an individual pixel generates the most pronounced electrical output. This can be attributed to the specific configuration of the MI layers, wherein the sensing coil is strategically centralized around the centroid of each pixel. Consequently, any potential cross-talk between neighboring pixels, instigated by tactile stimuli applied at the edges, can be effectively minimized. Taking a step further, the correlation between the pixel size and the electrical output was investigated in note S3. The experimental results point out that a BMAS with pixel dimensions of 0.55 cm by 0.55 cm can achieve comparable electrical output to a BMAS with pixel dimensions of 1 cm by 1 cm, by adjusting the gain of the tunable amplifier. Theoretical analysis indicates that the pixel size of BMAS can be further minimized to 0.23 cm by 0.23 cm to achieve distinguishable tactile cues, considering the noise level of ~0.035 V.

A salient attribute of the BMAS is the programmed magnetization profile of the MC layer. The ramifications of different programmed magnetization profiles on the discriminative capacity of the BMAS are comprehensively elucidated in note S4. Specifically, analysis and experimental results have confirmed that the programmed magnetization profile encodes an additional layer of information through the magnetization direction of a single pixel to augment the tactile perception of the BMAS. As a result, a substantial amount of diagonal two-point pressings can be identified by the directions of the obtained electrical signals. These distinctions are not possible when the MC layer adopts a uniform magnetization profile. Besides the diagonal two-point pressings, the BMAS can also identify complex two-point tactile stimuli such as the adjacent normal and shear forces. As displayed in note S5, the BMAS is capable of recognizing shear forces (including the direction) and adjacent normal forces on two neighboring pixels through the characteristics of activated channels, orientation of signals, and amplitude of the signals. This capability of the BMAS to recognize complex two-point tactile stimuli with different force types in a simplified architecture benefits from the proposed populational encoding strategy. The BMAS uses the populational response of neighboring pixels instead of the response of a single pixel to decode the perceived tactile information. The information encoding strategy using the polarity direction of the MC

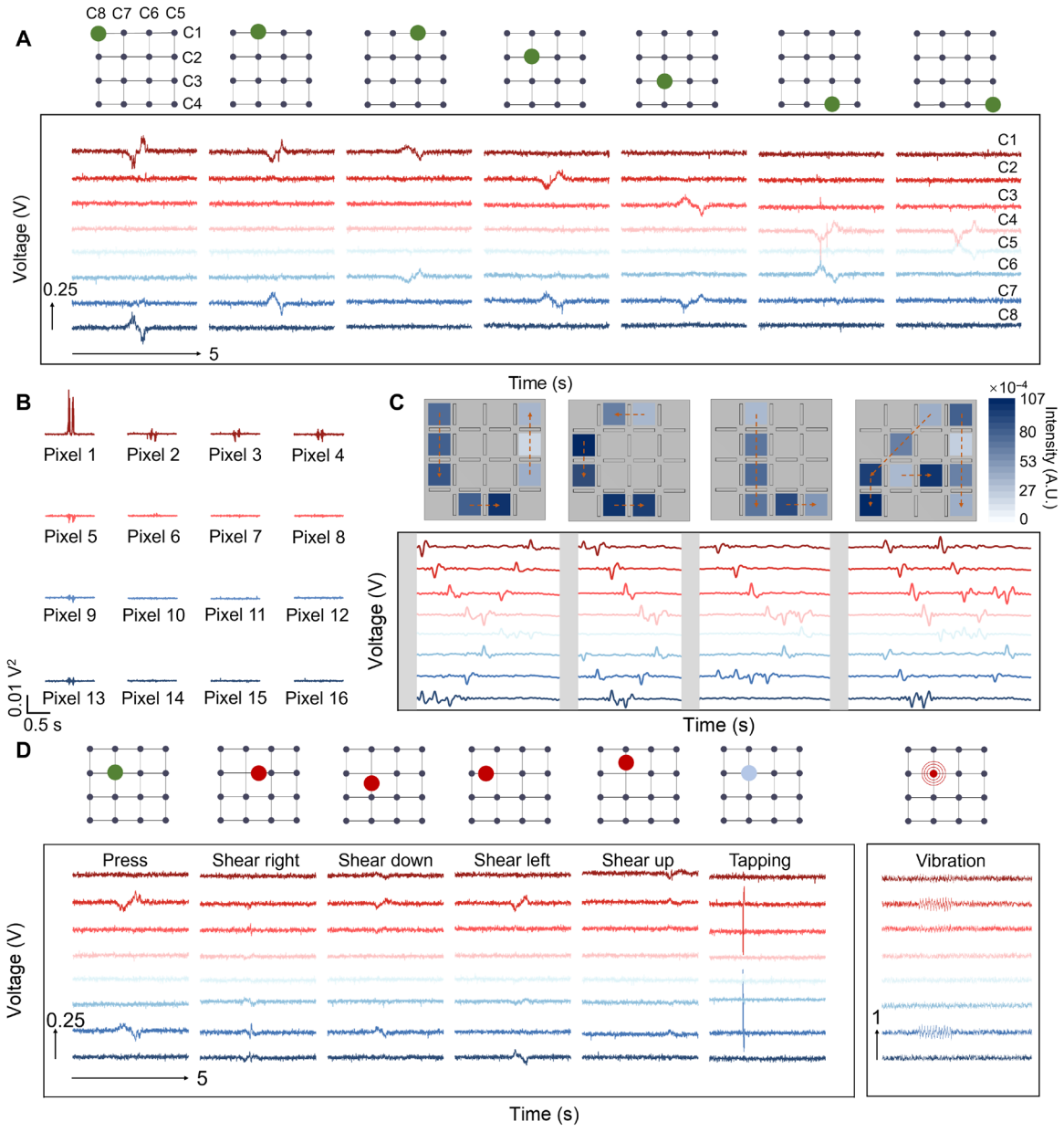

Fig. 3. Characterizing the perception capability of the magnetoelastic artificial skin. (**A**) Electrical output of the magnetoelastic artificial skin under normal press at different pixels. (**B**) The reconstructed electrical output of 16 pixels in the artificial skin from the eight stacked orthogonal channels. (**C**) Reconstructed tactile mapping of the signal output intensity when writing "U," "C," "L," and "A" and their corresponding voltage output profile using the eight stacked orthogonal channels. A.U., arbitrary units. (**D**) The electrical output of the magnetoelastic artificial skin under different tactile stimulation (press, shear right, shear down, shear left, shear, up, tapping, and vibration) at pixel 6.

layer also contributes to this recognition ability. It is worth mentioning that the obtained electrical signals of the BMAS under two different tactile stimuli on adjacent pixels are also distinctive from those obtained under a single tactile stimulus on a single pixel.

Underwater haptic sensing system

In the limited development of marine resources, notable environmental problems such as marine litter and ocean acidification have already emerged because of the lack of regulations and monitoring, causing a deleterious effect on the ocean's ecosystem (*22*, *23*). Today's ocean contains 26 million to 66 million tons of waste and most of them are trapped on the sea floor (*24*–*26*). These marine litters not only cause severe contamination of the ocean's ecosystem but also have a deleterious effect on sea creatures through entanglement, smothering, and ingestion. Eventually, the consequence of marine litter will be borne by the health of human beings evidenced by that microplastics have been found in human blood (*27*). Now, the removal of marine litter is heavily reliant on human divers, which is a risky and expensive undertaking (*28*). Very recently, AURs have emerged as an efficient technology for the curative measures of

underwater litter. However, there exist no accurate tactile sensing mechanisms in the current underwater robotics. As a result, current robotic recycling often leads to by-catch of benthic inhabitants, damage to sub-aquatic plants, and a crushing blow to the aquatic ecosystem.

The intrinsic waterproofness, multimodal perceptive capacity, self-powered capability, and simplified device structure make our BMAS-based haptic sensing system an appropriate candidate for this untapped yet far-reaching field of marine litter removal and recycling. Our BMAS can be attached to the grippers of the robotic arm to endow the aquatic robot with the capability of perception and cognition for sustainable marine litter recycling, which is safer, low cost, and highly efficient. Figure 4A depicts how autonomous aquatic robots

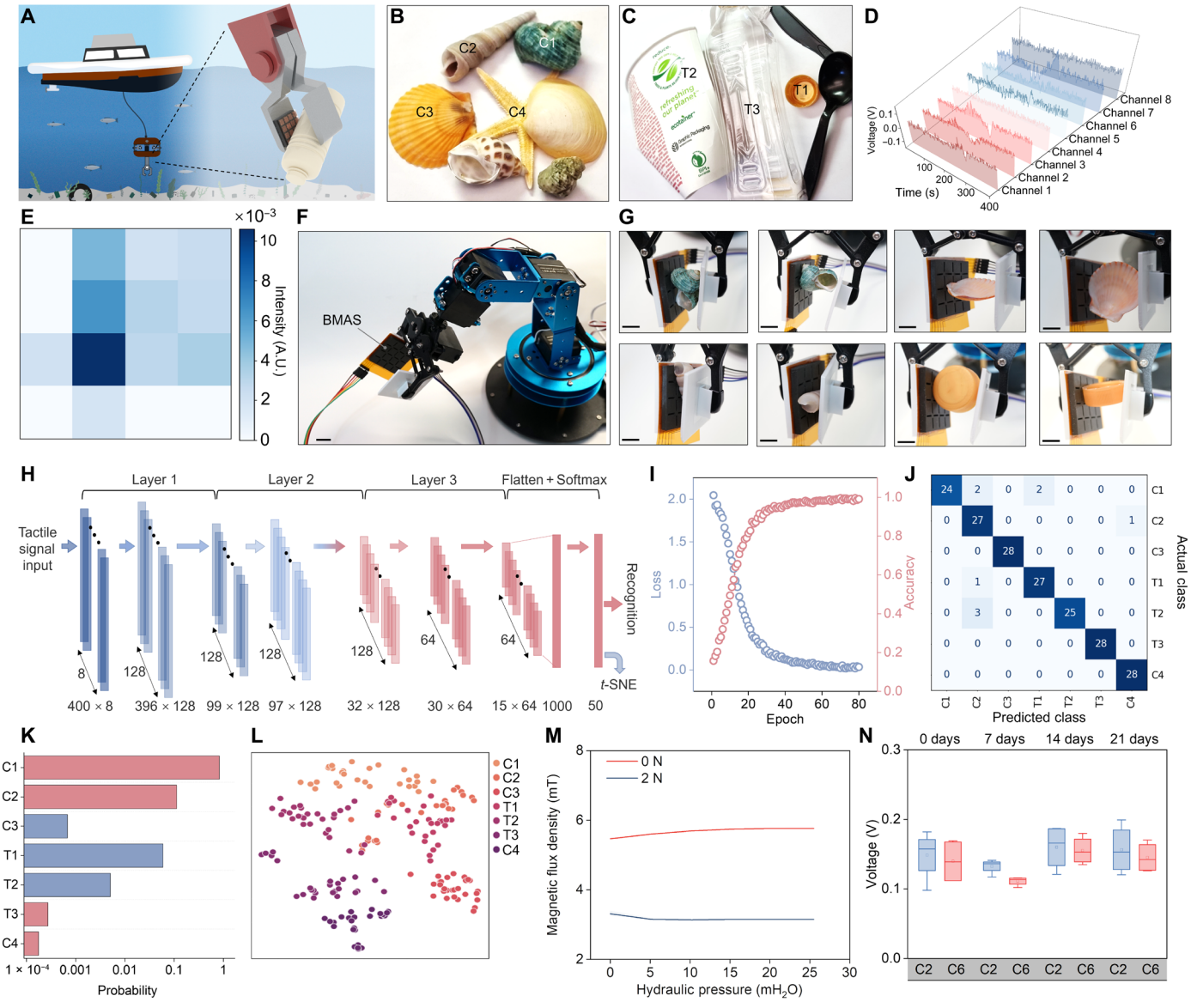

Fig. 4. The BMAS for underwater haptic sensing. (**A**) Schematic of the BMAS integrated on an autonomous aquatic robot for marine litter perception and recognition. (**B**) Image of the prepared ocean creatures includes a green sea mollusk shell (C1), a turritellidae (C2), a scallop (C3), and a starfish (C4). (**C**) Image of the ocean debris includes a bottle cap (T1), a paper cup (T2), and a plastic bottle (T3). (**D**) Electrical output of eight channels for the recognition of a green sea mollusk shell. (**E**) Reconstructed mapping of the sea mollusk shell. A.U., arbitrary units. (**F**) Photograph of a robotic arm integrated with the BMAS through a customized clamp. Scale bar, 2 cm. (**G**) Representative photograph of objects randomly clamped by the BMAS-equipped robotic arm. Scale bars, 1 cm. (**H**) Architecture of the 1D convolutional neural network used for underwater object recognition. (**I**) Evaluation of the recognition loss function and accuracy of the 1D-CNN deep learning algorithm in 80 epochs. (**J**) Confusion matrix for the seven types of marine creatures and marine litter tactile pattern recognition with randomly selected orientations and contact positions. Actual class refers to the collected data, and predicted class refers to predictions using the 1D-CNN deep learning algorithm. The total classification accuracy reaches ~95%. (**K**) Probability distribution of identifying the green sea mollusk shell after Softmax step in the 1D-CNN. (**L**) *t*-SNE visualization results of the data from the seven marine objects showing the clustering feature. (**M**) Magnetic flux density and magnetoelastic response of the BMAS under different hydraulic pressure conditions from 0 to 25 mH_2O. Data are means ± SD; $N = 3$. (**N**) Variation of voltage amplitude of the BMAS immersed in 3.5 wt % NaCl solution over a 21-day period. C2, channel 2; C6, channel 6. Data are means ± 1.5 interquartile range; $N = 4$.

can be used as an essential replacement for human divers for marine debris cleaning and recycling. To verify the proposed concept, the BMAS is used for the classification of four ocean creatures (a green sea mollusk, a turritellidae, a scallop, and a starfish in Fig. 4B) and three common ocean trashes (a bottle cap, a paper cup, and a plastic bottle in Fig. 4C) through tactile sensation. Figure 4 (D and E) and figs. S14 and S15 demonstrated the contact orientations, the electrical outputs, and the reconstructed signal mappings of the seven marine objects. It can be seen that each object generates a unique electrical output in the eight orthogonal channels and the reconstructed patterns are distinct. In real-world scenarios, the contact between the BMAS and objects would occur randomly, leading to unpredictable orientations and contact positions. To better mimic such real-world situations, a robotic clamp was designed to integrate the BMAS into a commercial robotic arm (Fig. 4F). The BMAS-equipped robotic arm was applied to clamp the objects including the green sea mollusk shell, turritellidae, scallop, and the bottle cap with randomly selected object orientations and object-BMAS contact positions (Fig. 4G and fig. S16). For the paper cup, plastic bottle, and starfish with dimensions larger than the moving range of the robotic clamp, these objects were directly pressed onto the BMAS with randomly selected orientations and contact positions as depicted in fig. S17. For each object, 148 voltage signal samples were collected and randomly divided into a training dataset (120 samples) and a test dataset (28 samples). A 1D-CNN deep learning algorithm with three hidden layers is further incorporated with the BMAS-based underwater haptic sensing system to realize robotic intelligence and accurate cognition (Fig. 4H). The obtained eight-channel electrical outputs were first normalized and then used as the input of the 1D-CNN, and the outputs were the predicted class of the contacted marine object. In the training period, the accuracy and loss function converge to 96% and 0.12 after 40 training epochs (Fig. 4I) with a batch size of 4 indicating the high efficiency and robustness of the 1D-CNN algorithm. Benefiting from the moderate model depth and the appropriate regularization, an overall classification accuracy of 95% in recognizing the marine objects with different sizes, shapes, and materials was achieved in the test dataset showing minimized overfitting, as evidenced by the confusion matrix in Fig. 4J. Figure 4K and fig. S18 further present the typical probability distribution of the seven sea objects following the applications of the Softmax layer in the 1D-CNN. All the detected target objects achieved a high probability close to 1, reflecting the robustness of the proposed algorithm and the underwater haptic sensing system. To better visualize the cognition process, we plotted the output (fig. S19 for the green sea mollusk) and kernel shapes (figs. S20 to S23) of the first convolutional layer in the trained 1D-CNN, which clearly demonstrated that different waveform shapes, amplitudes, phases, and frequencies were extracted and used for classification automatically without human artifacts. *t*-distributed stochastic neighbor embedding (*t*-SNE) algorithm, which is a nonlinear dimensionality reduction technique for embedding high-dimensional data, was also leveraged to represent the 1000-dimensional data obtained after the three convolutional layers in a 2D space. The result is visualized in Fig. 4L. Although some data points overlap with each other because of introduced randomness in object contact orientation and contact position, the clustering of data points is still discernible with distinctive boundaries verifying the feasibility of the deep learning–assisted BMAS for recognizing marine objects, which paves the way for marine litter recycling and the future exploration of marine resources in a sustainable manner.

The BMAS has been meticulously engineered for sustained operation in deep-sea environments, where both its sensibility and stability under such conditions are of paramount importance (*29*, *30*). Hence, additional experiments were performed to measure the magnetic flux density and magnetoelastic response of the BMAS in different hydraulic pressure conditions from 0 mH_2O to 25 mH_2O (meters of water) using a hydraulic container connected to a pressure gauge and a pressurization system. The corresponding results are displayed in Fig. 4M. It can be observed that both the magnetic flux density and the magnetoelastic response of the BMAS remain stable and consistent when hydraulic pressures of up to 25 mH_2O are applied. The experimental results confirmed that the BMAS can maintain its stability and sensibility in the deep-ocean environment. The remarkable sensibility and stability of the BMAS under high hydraulic pressure can be attributed to the nearly incompressible material properties inherent to the BMAS. Because the hydraulic pressure is an isotropic force applied to the BMAS, the incompressibility of the BMAS ensures that the net force applied to the device is almost zero, leading to the maintained sensibility of the BMAS in the deep-ocean environment. The long-term stability of the BMAS was also examined by monitoring its surface magnetic flux density and electrical response in both deionized (DI) water and 3.5 wt % NaCl solution over a period of 21 days. Figure S24A presents the temporal evolution of the surface magnetic flux density associated with the BMAS over 21 days. Concurrently, Fig. 4N and fig. S24B delineate the evolution of the voltage amplitude of the BMAS under a consistent pressing force of 1 N every 7 days after the BMAS was submerged in 3.5 wt % NaCl solution and DI water, respectively. Both the magnetic flux density and the amplitude of obtained voltage signals maintained a relatively consistent value during the testing period of 21 days. These results indicate that the BMAS maintains a stable performance in both aquatic and simulated sea environments. The excellent long-term stability of the BMAS can be ascribed to two contributions. First, the insulating property of the BMAS effectively prevents the formation of microcells and therefore inhibits the occurrence of micro-battery corrosion activities (*31*). Second, while some micromagnets on the BMAS surface without polymer protection might experience minor corrosion, the waterproof polymer matrix shields the majority of micromagnets embedded within it from corrosion. Because the magnetoelastic effect manifests as an inherent bulk characteristic rather than a surface attribute of the BMAS, any minor surface corrosion will not compromise the performance of the BMAS. Overall, the BMAS is proven to have stable sensibility and long-term performance stability in simulated deep-ocean environments. These results fortify the robustness and reliability of using the BMAS as an underwater haptic sensor in exploring future marine recourses.

Wearable human-computer interface

The BMAS can be further generalized to the field of wearable human-machine interfaces. In this regard, our BMAS uses its different pixels for the robotic arm control and the multiplexed tactile modality of a single pixel to play the "snake" game on the personal computer simultaneously (fig. S25). Specifically, the normal presses on 16 pixels of the artificial skin were programmed into commands to control a 6–degree-of-freedom (DOF) robotic arm with Pixels 1–12 to control a single movement of each servo motor, Pixels 13–15 to enable a complex movement using a combination of multiple servo motors, and Pixel 16 for resetting the robotic arm to its initial position (fig. S26, A and B). Application of the 1D-CNN substantially improved

the recognition performance of the normal press, as evidenced by the 100% accuracy achieved using the test dataset in fig. S27. Combining the deep learning algorithm and the BMAS, real-time dexterous control of the robotic arm to manipulate a glass vital has been realized (fig. S26B and movie S2). An exclusive advantage of the magnetoelastic artificial skin is the multiplexed tactile modality on its single pixel. Complex human-machine interaction tasks therefore can be accomplished using a single taxel compared to six taxels required using traditional sensor arrays (*32*), which substantially reduces the system complexity. To demonstrate this point, we applied the 1D-CNN algorithm to enhance the recognition of normal press, tapping, vibration, and four shear deformations of Pixel 6. As illustrated in fig. S28A, an overall classification accuracy of 95% can be achieved by benefiting from the stackable device architecture, the rich information encoded through the magnetoelastic effect, and the powerful performance of 1D-CNN. Taking a step further, the four shear deformations (shear up, shear right, shear down, and shear left) of Pixel 6 were successfully utilized to play a classical game of "Snake" developed with Python code (fig. S28B and movie S3), in which users control the direction of the snake (shear right for turn right, shear down for turn down, shear left for turn left, and shear up for turn up in fig. S28, C to F) to eat a randomly distributed food. It is worth mentioning that the BMAS can control the robotic arm and play the computer game without disruption from each other. With more advanced designs of each taxel's functionality and close-loop control, the magnetoelastic artificial skin could serve as an important basis for more complicated human-machine interactions such as robotic VR and remote medical surgery.

DISCUSSION

The BMAS is different from the traditional tactile sensor arrays of its kind in two aspects. First, the BMAS has a stackable architecture. The deep penetration depth of the magnetoelastic effect, measured as 3.69 mm, allows multiple stacked MI layers to receive the magnetic flux density variation with a decay of only 4% per subsequent MI layer. By strategically refining the substrate thickness of the MI layer to 0.05 mm, theoretical projections suggest that the attenuation rate can potentially be mitigated to 1% for each MI layer. This opens another dimension of freedom in designing artificial skin in the vertical direction and proposes a previously unidentified field of 3D electrode design for tactile sensing. In contrast, traditional row-by-column configured tactile sensor arrays did not support the stackable architecture because their sensing mechanisms require direct deformation of the sensing channels so that tactile stimulation applied on the top taxel cannot effectively transmit to the bottom one. It should be also mentioned that the stackable architecture also enables the reconfigurability of the artificial skin so that its sensing layers can be rearranged and reassembled with maximum freedom to adapt to versatile tactile tasks (*33*).

Second, benefiting from the large receptive field of the magnetic field and the design of sensory channels terminating on multiple coil sensing elements, a single taxel of the magnetoelastic artificial skin can perceive and recognize multiple tactile stimulations such as shear force, normal force, and vibration. As a result, 8 sensory channels in the artificial skin accomplish the task of 64 individual channels with the assistance of the 1D-CNN deep learning algorithm. Such a feature has not been realized in conventional row-by-column configured tactile sensors limited by their sensing mechanisms.

In addition, traditional ones often confront difficulties in multipixel detection. Although some algorithms can be used to reconstruct the signal in every single taxel, they cannot realize the same mapping capability of the individually addressable tactile panels. The BMAS can overcome this grand challenge and realize individually addressable haptic sensing in an unorthodox approach. As illustrated in fig. S29 and notes S4 and S5, the perception of a complex two-point tactile stimulation can be distinguished by the BMAS with an additional MI layer or the programming of the MC layer, showing the advancement of the magnetoelastic effect-based stackable architecture for tactile sensing.

A more comprehensive comparison of the BMAS to piezoresistive, capacitive, piezoelectric, and triboelectric tactile sensors is summarized in table S1 and note S6. Overall, the BMAS holds advantages of the intrinsic waterproof sensing mechanism, the realization of multimodality using minimal sensing channels, stackability, and reconfigurability benefiting from the expansive perception field of the magnetoelastic effect in soft systems.

Last, the total cost for the magnetoelastic artificial skin is projected to be approximately $21.08 (table S2). It is worth noting that a substantial portion of this cost is attributed to the associated circuits, which may be further reduced through scalable production. Consequently, the magnetoelastic artificial skin presents an economically viable solution for multichannel multimodal haptic sensing, holding potential for a diverse range of applications.

In summary, we present a BMAS for underwater haptic sensing that enables intelligent tactile perception and cognition in aquatic environments. With the assistance of 1D-CNN, it was demonstrated to perform underwater object recognition and marine litter recycling. Benefiting from its 3D stackable design, the BMAS-based underwater haptic sensing holds a collection of compelling features, including low cost, high scalability, self-powered operation capability, and multiplexed sensing modality for force self-decoupling. This research provides a promising and alternative approach to tactile sensor design suitable for underwater robot sensing, including deep-sea biological sampling and deep-sea construction. It is a milestone toward sustainable marine resource exploitation.

MATERIALS AND METHODS

Fabrication of the magnetoelastic artificial skin

To fabricate the MC layer, the NdFeB micromagnets were first mixed thoroughly with the Ecoflex 00-30 (Smooth-on Inc.) with a weight ratio of 1:1. The mixture was then poured into a special mold (40 mm by 40 mm by 3.5 mm) with the design of orthogonal groove structures (7 mm by 1 mm by 1.75 mm). Subsequently, the mold together with the mixture composite was put in an oven of 70°C for 3 hours. Last, the MC layer was taken out from the oven, folded into an origami shape of 20 mm by 20 mm by 14 mm, and magnetized by an impulse magnetizer (IM-10-30, ASC Scientific). A thin flexible printed circuit board (FPCB) formed with conductive tracks served as the basis for the fabrication of the MI layer. The FPCB itself consisted of a transparent polyethylene terephthalate (PET; 220 μm) substrate with patterned traces of copper (18 μm thick) on both top and bottom surfaces, each encapsulated with an insulating PET film (20 μm thick) using a layer of silicone adhesive (25 μm thick) in between. Each copper line in the coil sensing element is 254 μm wide and separated by a gap of 254 μm. Each coil sensing element is 9.398 mm long and 9.398 mm wide and contains eight turns of copper line. Four coil

sensing elements are connected by four vertical-interconnected accesses to form an independent sensory channel.

Characterization of the BMAS

The morphology of the MC layer in the BMAS was characterized by scanning electron microscopy (Zeiss, supra 40VP). The mechanical stress-strain curve was measured using an electromechanical testing system (Instron 5564) with a stretching speed of 0.083 mm s^{-1}. Young's modulus of the MC layer was derived by fitting the tested curves using a neo-Hookean model. The magnetic flux density-stress curve was obtained using a customized system with a digital Hall sensor (Tunkia, TD8620) and a force gauge. Mapping of the magnetic flux density of the MC layer with and without stress was obtained using a customized system using the Hall sensor and two-axis motion platform. A 3.1-mm plastic plate is inserted between the MC layer and the Hall sensor to apply stress and ensure a consistent comparison. Current signals of a single pixel on the magnetoelastic artificial skin were measured by the joint usage of two current pre-amplifiers (SR570, Stanford Research). Multichannel measurements were performed using a customized measuring circuit composed of a multiplexer (74HC4067), a commercial amplifier, and a microcontroller (Adafruit, Trinket M0). Reconstruction of the signal mapping was conducted by multiplying the electrical outputs of the top MI layer by the electrical outputs of the bottom MI layer. NaCl (≥99%) for the long-term stability characterization was purchased from Sigma-Aldrich.

1D convolutional neural network

To enable the intelligence of the BMAS and an accurate classification rate, a 1D-CNN is adopted using the TensorFlow framework. The 1D-CNN has three hidden convolutional layers followed by two fully connected layers. Each convolutional layer has 128, 128, and 64 neurons, and the kernel sizes used in each convolutional layer are 5, 3, and 3, respectively. Rectified linear units (ReLU) were used for activation and nonlinearity after the convolutional layers. Dropout layers were used in the model to prevent overfitting. After each convolutional layer, a Maxpooling layer was added to provide an abstracted form of data structure and reduce the computational cost. The first fully connected layer includes 1000 neurons with ReLU activation, and the second fully connected layer includes 7 neurons with softmax activation to output the final classification result. For the underwater object recognition, 840 (120 × 7) sets of data were fed into the 1D-CNN as the input in the training period. One hundred and ninety-six (28 × 7) sets of data were used as the test dataset. When combining the 1D-CNN with the *t*-SNE to visualize the high-dimensional data, an additional linear layer of 50 neurons was added before the softmax classification since this step helps suppress noises and speed up the computation of pairwise distances between samples.

Robotic arm control and snake gameplay

A six DOF robotic arm (LeArm) was used for the demonstration of human-robotic interaction. For each DOF, two pixels on the magnetoelastic skin were programmed to control the movement of the servo motor. The additional four pixels were used for the combined commands and a reset button. For the real-time robotic control, the 1D-CNN was first trained using 1020 sets of data; then, a customized program was used to partition the real-time electrical output of the magnetoelastic skin into signals with equal length consecutively. These signals were then fed into the 1D-CNN and output a pixel number representing the different commands for the robotic arm. The number is then sent to an Arduino UNO microcontroller board to control the corresponding movement of the robotic arm in real time. The snake game is written in Python language using the Pygame library. The 1D-CNN to control the direction of the snake was trained using 420 sets of data. Real-time electrical outputs of the magnetoelastic artificial skin were cut into signals with equal lengths and fed into the 1D-CNN, which generates the classified result and controls the direction of the snake in situ.

Supplementary Materials

This PDF file includes:

Figs. S1 to S42
Tables S1 and S2
Notes S1 to S6
Legends for movies S1 to S3
References

Other Supplementary Material for this manuscript includes the following:

Movies S1 to S3

REFERENCES AND NOTES

1. L. A. Levin, D. J. Amon, H. Lily, Challenges to the sustainability of deep-seabed mining. *Nat. Sustain.* **3**, 784–794 (2020).
2. R. Danovaro, C. Corinaldesi, A. Dell'Anno, P. V. R. Snelgrove, The deep-sea under global change. *Curr. Biol.* **27**, R461–R465 (2017).
3. B. T. Phillips, K. P. Becker, S. Kurumaya, K. C. Galloway, G. Whittredge, D. M. Vogt, C. B. Teeple, M. H. Rosen, V. A. Pieribone, D. F. Gruber, R. J. Wood, A dexterous, glove-based teleoperable low-power soft robotic arm for delicate deep-sea biological exploration. *Sci. Rep.* **8**, 14779 (2018).
4. S. Sundaram, P. Kellnhofer, Y. Li, J.-Y. Zhu, A. Torralba, W. Matusik, Learning the signatures of the human grasp using a scalable tactile glove. *Nature* **569**, 698–702 (2019).
5. S. C. B. Mannsfeld, B. C. K. Tee, R. M. Stoltenberg, C. V. H. H. Chen, S. Barman, B. V. O. Muir, A. N. Sokolov, C. Reese, Z. Bao, Highly sensitive flexible pressure sensors with microstructured rubber dielectric layers. *Nat. Mater.* **9**, 859–864 (2010).
6. H. Sun, K. J. Kuchenbecker, G. Martius, A soft thumb-sized vision-based sensor with accurate all-round force perception. *Nat. Mach. Intell.* **4**, 135–145 (2022).
7. X. Wang, W.-Z. Song, M.-H. You, J. Zhang, M. Yu, Z. Fan, S. Ramakrishna, Y.-Z. Long, Bionic single-electrode electronic skin unit based on piezoelectric nanogenerator. *ACS Nano* **12**, 8588–8596 (2018).
8. Y. Luo, X. Xiao, J. Chen, Q. Li, H. Fu, Machine-learning-assisted recognition on bioinspired soft sensor arrays. *ACS Nano* **16**, 6734–6743 (2022).
9. H. Niu, H. Li, S. Gao, Y. Li, X. Wei, Y. Chen, W. Yue, W. Zhou, G. Shen, Perception-to-cognition tactile sensing based on artificial-intelligence-motivated human full-skin bionic electronic skin. *Adv. Mater.* **34**, 2202622 (2022).
10. F. R. Hogan, J. Ballester, S. Dong, A. Rodriguez, in 2020 IEEE international conference on robotics and automation (ICRA) (2020), pp. 8863–8869.
11. Y. Yan, Z. Hu, Z. Yang, W. Yuan, C. Song, J. Pan, Y. Shen, Soft magnetic skin for super-resolution tactile sensing with force self-decoupling. *Sci. Robot.* **6**, eabc8801 (2021).
12. M. Zhu, T. He, C. Lee, Technologies toward next generation human machine interfaces: From machine learning enhanced tactile sensing to neuromorphic sensory systems. *Appl. Phys. Rev.* **7**, 031305 (2020).
13. V. Nguyen, R. Yang, Effect of humidity and pressure on the triboelectric nanogenerator. *Nano Energy* **2**, 604–608 (2013).
14. Y. Gu, T. Zhang, J. Li, C. Zheng, M. Yang, S. Li, A new force-decoupling triaxial tactile sensor based on elastic microcones for accurately grasping feedback. *Adv. Intell. Syst.* **5**, 2200321 (2023).
15. P. Wilkinson, R. Millington, *Skin (Digitally Printed Version Ed.)*. (Cambridge Univ. Press, 2009).
16. V. E. Abraira, D. D. Ginty, The sensory neurons of touch. *Neuron* **79**, 618–639 (2013).
17. A. Chortos, J. Liu, Z. Bao, Pursuing prosthetic electronic skin. *Nat. Mater.* **15**, 937–950 (2016).
18. H. E. Wheat, L. M. Salo, A. W. Goodwin, Cutaneous afferents from the monkeys fingers: Responses to tangential and normal forces. *J. Neurophysiol.* **103**, 950–961 (2009).
19. Y. Zhou, X. Zhao, J. Xu, Y. Fang, G. Chen, Y. Song, S. Li, J. Chen, Giant magnetoelastic effect in soft systems for bioelectronics. *Nat. Mater.* **20**, 1670–1676 (2021).
20. T. Kim, J. Kim, I. You, J. Oh, S.-P. Kim, U. Jeong, Dynamic tactility by position-encoded spike spectrum. *Sci. Robot.* **7**, eabl5761 (2022).

21. J. Y. Wu, P. P. Pancham, T. Y. Hsu, A. Mukherjee, C. Y. Lo, in *2022 IEEE Sensors* (2022), pp. 1–3.
22. N. Bellou, C. Gambardella, K. Karantzalos, J. G. Monteiro, J. Canning-Clode, S. Kemna, C. A. Arrieta-Giron, C. Lemmen, Global assessment of innovative solutions to tackle marine litter. *Nat. Sustain.* **4**, 516–524 (2021).
23. M. Visbeck, Ocean science research is key for a sustainable future. *Nat. Commun.* **9**, 690 (2018).
24. F. Madricardo, M. Ghezzo, N. Nesto, W. J. Mc Kiver, G. C. Faussone, R. Fiorin, F. Riccato, P. C. Mackelworth, J. Basta, F. De Pascalis, A. Kruss, A. Petrizzo, V. Moschino, How to deal with seafloor marine litter: An overview of the state-of-the-art and future perspectives. *Front. Mar. Sci.* **7**, (2020).
25. J. G. B. Derraik, The pollution of the marine environment by plastic debris: A review. *Mar. Pollut. Bull.* **44**, 842–852 (2002).
26. J. R. Jambeck, R. Geyer, C. Wilcox, T. R. Siegler, M. Perryman, A. Andrady, R. Narayan, K. L. Law, Plastic waste inputs from land into the ocean. *Science* **347**, 768–771 (2015).
27. A. D. Vethaak, J. Legler, Microplastics and human health. *Science* **371**, 672–674 (2021).
28. A. Spengler, M. F. Costa, Methods applied in studies of benthic marine debris. *Mar. Pollut. Bull.* **56**, 226–230 (2008).
29. M. Zhang, S. Fang, J. Nie, P. Fei, A. E. Aliev, R. H. Baughman, M. Xu, Self-powered, electrochemical carbon nanotube pressure sensors for wave monitoring. *Adv. Funct. Mater.* **30**, 2004564 (2020).
30. Y. Cheng, C. Guo, S. Li, K. Deng, J. Tang, Q. Luo, S. Zhang, Y. Chang, T. Pan, Aquatic skin enabled by multi-modality iontronic sensing. *Adv. Funct. Mater.* **32**, 2205947 (2022).
31. X. Hou, L. Gao, Z. Cui, J. Yin, Corrosion and protection of metal in the seawater desalination. *IOP Conf.: Earth Environ. Sci.* **108**, 022037 (2018).
32. Y. Gao, B. Zhang, Y. Liu, K. Yao, X. Huang, J. Li, T. H. Wong, Y. Huang, J. Li, J. Zhou, M. Wu, H. Li, Z. Gao, W. Park, C. K. Yiu, H. Jia, R. Shi, D. Li, X. Yu, Mechanoreceptor inspired electronic skin for multi-modal tactile information decoding. *Adv. Mater. Technol.* **8**, 2200759 (2022).
33. C. Choi, H. Kim, J.-H. Kang, M.-K. Song, H. Yeon, C. S. Chang, J. M. Suh, J. Shin, K. Lu, B.-I. Park, Y. Kim, H. E. Lee, D. Lee, J. Lee, I. Jang, S. Pang, K. Ryu, S.-H. Bae, Y. Nie, H. S. Kum, M.-C. Park, S. Lee, H.-J. Kim, H. Wu, P. Lin, J. Kim, Reconfigurable heterogeneous integration using stackable chips with embedded artificial intelligence. *Nat. Electron.* **5**, 386–393 (2022).
34. Y. Jung, D. G. Lee, J. Park, H. Ko, H. Lim, Piezoresistive tactile sensor discriminating multidirectional forces. *Sensors (Basel)* **15**, 25463–25473 (2015).
35. Y. Luo, Y. Li, P. Sharma, W. Shou, K. Wu, M. Foshey, B. Li, T. Palacios, A. Torralba, W. Matusik, Learning human–environment interactions using conformal tactile textiles. *Nat. Electron.* **4**, 193–201 (2021).
36. J. Zhang, H. Yao, J. Mo, S. Chen, Y. Xie, S. Ma, R. Chen, T. Luo, W. Ling, L. Qin, Z. Wang, W. Zhou, Finger-inspired rigid-soft hybrid tactile sensor with superior sensitivity at high frequency. *Nat. Commun.* **13**, 5076 (2022).
37. S. Hu, W. Lu, H. Li, X. Shi, Z. Peng, X. Cao, Model-driven triboelectric sensors for multidimensional tactile perception. *Nano Energy* **114**, 108658 (2023).

Acknowledgments

Funding: The authors acknowledge the Henry Samueli School of Engineering and Applied Science and the Department of Bioengineering at the University of California, Los Angeles for the startup support. J.C. also acknowledges the Vernroy Makoto Watanabe Excellence in Research Award at the UCLA Samueli School of Engineering, the Brain & Behavior Research Foundation Young Investigator Grant (grant number 30944), the Catalyzing Pediatric Innovation Grant (grant number 47744) from the West Coast Consortium for Technology & Innovation in Pediatrics, Children's Hospital Los Angeles, the NIH National Center for Advancing Translational Science UCLA CTSI (grant number KL2TR001882), the American Heart Association Innovative Project Award (award ID 23IPA1054908), the American Heart Association Transformational Project Award (award ID 23TPA1141360), and the American Heart Association's Second Century Early Faculty Independence Award (award ID 23SCEFIA1157587), and the Office of Naval Research Young Investigator Award (award ID N00014-24-1-2065).

Author contributions: Conceptualization: Y.Z. and J.C. Methodology: Y.Z., X.Z., J.C., J.X., T.T., G.C., and J.L. Investigation: Y.Z. and X.Z. Visualization: Y.Z., X.Z., J.C. Funding acquisition: J.C. Project administration: J.C. Supervision: J.C. Writing (original draft): Y.Z., X.Z., and J.C. Writing (review and editing): Y.Z. and J.C. **Competing interests:** The authors declare that they have no competing interest. **Data and materials availability:** All data needed to evaluate the conclusions in the paper are present in the paper and/or the Supplementary Materials.

Submitted 19 July 2023
Accepted 5 December 2023
Published 5 January 2024
10.1126/sciadv.adj8567